ACS Energy LETTERS

Cite This: ACS Energy Lett. 2018, 3, 2504−2512

http://pubs.acs.org/journal/aelccp

LETTER

# Vacancy-Driven $Na^+$ Superionic Conduction in New Ca-Doped $Na_3PS_4$ for All-Solid-State Na-Ion Batteries

Chang Ki Moon,[†,⊥] Hyun-Jae Lee,[‡,⊥] Kern Ho Park,[†] Hiram Kwak,[†] Jongwook W. Heo,[§] Keunsu Choi,[‡] Hyemi Yang,[‡] Maeng-Suk Kim,[‡] Seung-Tae Hong,[§] Jun Hee Lee,*[,‡] and Yoon Seok Jung*[,†]

[†]Department of Energy Engineering, Hanyang University, Seoul 04763, South Korea

[‡]School of Energy and Chemical Engineering, UNIST (Ulsan National Institute of Science and Technology), Ulsan 44919, South Korea

[§]Department of Energy Science and Engineering, DGIST (Daegu Gyeongbuk Institute of Science and Technology), Daegu 42988, South Korea

Supporting Information

**ABSTRACT:** Mechanically sinterable sulfide $Na^+$ superionic conductors are key to enabling room-temperature-operable all-solid-state Na-ion batteries (ASNBs) for large-scale energy storage applications. To date, few candidates can fulfill the requirement of a high ionic conductivity of ≥1 mS $cm^{-1}$ using abundant, cost-effective, and nontoxic elements. Herein, the development of a new $Na^+$ superionic conductor, Ca-doped cubic $Na_3PS_4$, showing a maximum conductivity of ∼1 mS $cm^{-1}$ at 25 °C is described. Complementary analyses using conductivity measurement by the AC impedance method, $^{23}Na$ nuclear magnetic resonance spectroscopy, and density functional theory calculations reveal that the aliovalent substitution of $Na^+$ in $Na_3PS_4$ with $Ca^{2+}$ renders a cubic phase with Na vacancies, which increases the activation barriers but drastically enhances Na-ion diffusion. It is demonstrated that $TiS_2$/Na−Sn ASNBs employing Ca-doped $Na_3PS_4$ exhibit a high charge capacity of 200 mA h $g^{-1}$ at 0.06*C*, good cycling performance, and higher rate capability than those employing undoped cubic $Na_3PS_4$.

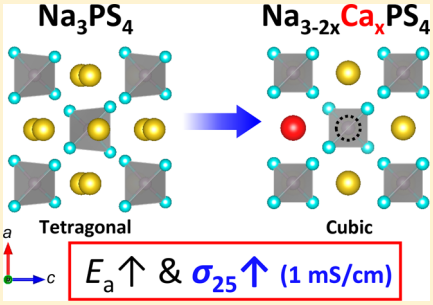




Lithium-ion batteries have become ubiquitous in mobile devices owing to their high energy and power densities.[1,2] At present, their application in large-scale energy storage such as battery-driven electric vehicles and grid-scale energy storage is on the verge of an explosive expansion.[1,2] However, serious safety concerns originating from the use of flammable organic liquid electrolytes[3−5] and the cost issues related to Li (its limited abundance, recent rapid increase in the price of $Li_2CO_3$, and geologically uneven distribution)[6,7] are serious obstacles. In this regard, solidifying electrolytes using inorganic $Na^+$ superionic conductors can be the ultimate solution.[8−15] Although Na $\beta''$-alumina (ionic conductivity of ∼$10^{-2}$ S $cm^{-1}$ at room temperature) was the first commercialized Na-ion conductor employed in Na−S batteries for large-scale energy storage systems,[16] oxide materials may not be suitable to fabricate room-temperature-operable all-solid-state Na-ion batteries (ASNBs) because a deteriorating high-temperature sintering process is necessary to obtain two-dimensional contact with active materials.[8,10,13,17] In contrast, sulfide materials are mechanically sinterable owing to their more covalent bonds.[8−10,13,18] Moreover, high conductivities reaching the order of $10^{-4}$−$10^{-3}$ S $cm^{-1}$ at room temperature have been achieved for several sulfide solid electrolyte (SE) materials.[8−10,18−20]

Tatsumisago and co-workers developed the first sulfide $Na^+$ superionic conductor, cubic $Na_3PS_4$ (c-$Na_3PS_4$), showing a conductivity of 0.2 mS $cm^{-1}$ at room temperature, which was in contrast to a previously reported tetragonal $Na_3PS_4$ (t-$Na_3PS_4$, 0.001 mS $cm^{-1}$).[8,21] By X-ray structural analysis, the high conductivity of the cubic phase was attributed to the existence of three-dimensional (3D) ionic conduction pathways between the Na1 and Na2 sites.[22] Moreover, first-principles investigations showed that the occupancy of the Na2 site (or Na disorder) was key to the high ionic conductivity of c-$Na_3PS_4$.[23] Since then, extensive efforts for further development have been undertaken.

The first strategy was an aliovalent substitution of P. The replacement of P in c-$Na_3PS_4$ with 6 mol % Si resulted in an ionic conductivity of 0.74 mS $cm^{-1}$.[24] It was explained that the excess Na led to an increased occupancy in the interstitial Na2

Received: August 13, 2018
Accepted: September 14, 2018




DOI: 10.1021/acsenergylett.8b01479
ACS Energy Lett. 2018, 3, 2504−2512

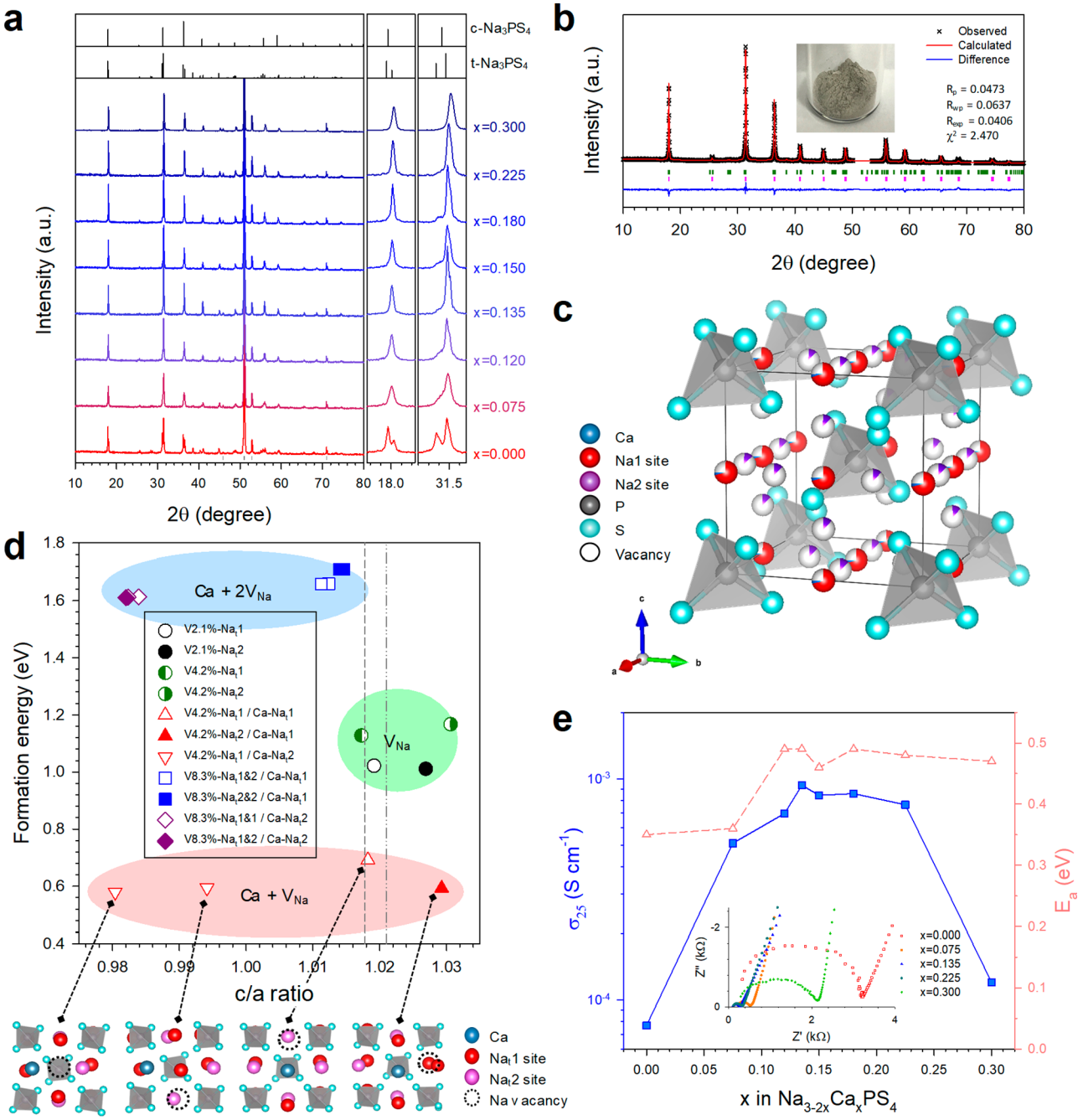


**Figure 1. Characterization of Ca-doped $Na_3PS_4$ ($Na_{3-2x}Ca_xPS_4$ ($0 \le x \le 0.300$)) prepared at 700 °C. (a) Powder XRD patterns for $Na_{3-2x}Ca_xPS_4$. Bragg positions for Be window (gray vertical lines) are also shown at the bottom. (b) X-ray Rietveld refinement profile for $Na_{2.730}Ca_{0.135}PS_4$. The photograph of $Na_{2.730}Ca_{0.135}PS_4$ powders is provided in the inset. (c) Crystal structure of cubic $Na_{2.730}Ca_{0.135}PS_4$ with the unit cell outlined. (d) Calculated formation energy of $Na_3PS_4$ as a function of $c/a$ ratio by varying Ca doping and $V_{Na}$ concentration. The details about the symbols are shown in Table 1. The short-dashed line (---) and the dashed−dotted line (−··−) indicate the $c/a$ ratios for t-$Na_3PS_4$ obtained by the experiment[21] and calculation, respectively. (e) Na-ion conductivities at 25 °C and activation energies for $Na_{3-2x}Ca_xPS_4$. Nyquist plots are shown in the inset of panel e.**

site, increasing the conductivity.[22,24] This reasoning was supported by the subsequent density functional theory (DFT) calculation results.[23] The second strategy was an isovalent substitution of P or S in $Na_3PS_4$ with larger elements of Sb, As, and Se; high ionic conductivities of ~1 mS $cm^{-1}$ were achieved for tetragonal $Na_3SbS_4$,[9,25,26] tetragonal $Na_3P_{0.62}As_{0.38}S_4$,[27] and cubic $Na_3PSe_4$.[28,29] By exploration of four-element systems, a new structural class of superionic conductors, $Na_{4-x}Sn_{1-x}Sb_xS_4$[19] and $Na_{11}Sn_2PS_{12}$,[30,31] was also identified. However, the introduction of heavy elements, such as Sb, Sn, Se, and As, for SEs would result in lowering the specific energy density of ASNBs. Also, toxicity (or environmental effects) and abundance of the elements should be considered in designing $Na^+$ superionic conductor materials for their practical application.[13] The last strategy was to generate Na vacancies. Contrary to the initial assumption that the high ionic conductivity of c-$Na_3PS_4$ originates from its cubic structure,[8] DFT and molecular dynamics (MD) calculations



DOI: 10.1021/acsenergylett.8b01479
ACS Energy Lett. 2018, 3, 2504−2512

Table 1. Calculated Vacancy and Ca Doping Formation Energy of $Na_3PS_4$, Varied by Ca Doping and $V_{Na}$ Concentration

| Composition | Concentration of Na vacancy (%) | Symbol in Figure 1d | Vacancy site[a] | Ca site | Formation energy (eV) |
|---|---|---|---|---|---|
| $Na_{2.9375}PS_4$ | 2.08 | ○ | $Na_t1$ | - | 1.022 |
| | | ● | $Na_t2$ | - | 1.011 |
| $Na_{2.8750}PS_4$ | 4.17 | ◐ | $Na_t1$ | - | 1.128 |
| | | ◑ | $Na_t2$ | - | 1.167 |
| $Na_{2.750}Ca_{0.125}PS_4$ | 4.17 | △ | $Na_t1$ | $Na_t1$ | 0.692 |
| | | ▲ | $Na_t2$ | $Na_t1$ | 0.593 |
| | | ▽ | $Na_t1$ | $Na_t2$ | 0.579, 0.594 |
| $Na_{2.625}Ca_{0.125}PS_4$ | 8.33 | □ | $Na_t1$ & 2 | $Na_t1$ | 1.659, 1.658 |
| | | ■ | $Na_t2$ & 2 | $Na_t1$ | 1.709, 1.710 |
| | | ◇ | $Na_t1$ & 1 | $Na_t2$ | 1.613, 1.612 |
| | | ◆ | $Na_t1$ & 2 | $Na_t2$ | 1.611 |

[a]Based on tetragonal structure.

showed that a stoichiometric c-$Na_3PS_4$ is a poor ionic conductor and that the introduction of Na vacancies drastically enhances the ionic conductivity.[23,29,32,33] It was predicted that 2% Na vacancies in t-$Na_3PS_4$ ($Na_{2.94}PS_4$) rendered the increase in $Na^+$ tracer diffusivity by more than order of magnitude (from $1 \times 10^{-7}$ to $2.3 \times 10^{-6}$ $cm^2$ $s^{-1}$).[33] Furthermore, it was reported that the formation of Na vacancies by aliovalent substitution of S in $Na_3PS_4$ with Cl, which resulted in the formation of tetragonal $Na_{2.9375}PS_{3.9375}Cl_{0.0625}$, could achieve a high conductivity of 1 mS $cm^{-1}$.[34] However, it should be noted that this value was obtained using spark-plasma-sintered pellets, leading to significantly reduced grain-boundary and interparticle resistances compared with those of pellets prepared by conventional cold pressing.[35,36] Considering the strong emphasis on Na vacancies in $Na^+$ superionic conductors,[23,25,29−34,37,38] it is surprising that there has been only one experimental case investigating the formation of vacancies by aliovalent substitution of $Na_3PS_4$, Cl-doped $Na_3PS_4$, in this field.[34]

Herein, we report the development of new $Na^+$ superionic conductors, Ca-doped cubic $Na_3PS_4$. Aliovalent substitution of $Na^+$ in t-$Na_3PS_4$ with $Ca^{2+}$ results in the cubic phase ($Na_{3-2x}Ca_xPS_4$) and creates Na vacancies, drastically enhancing the ionic conductivity up to ∼1 mS $cm^{-1}$ at 25 °C ($x$ = 0.135, using cold-pressed pellet). It is emphasized that the high conductivity of 1 mS $cm^{-1}$ in this work is obtained using earth-abundant and environmentally benign elements (Na, Ca, P, and S). The fast ionic movements in Ca-doped c-$Na_3PS_4$ are investigated by $^{23}Na$ solid-state nuclear magnetic resonance (NMR) spectroscopy. DFT calculations confirm the evolution of the cubic structure by Ca doping, the excellent Ca dopability, and the increased activation barrier for migration of Na vacancies by Ca doping. Also, DFT-based MD (DFTMD) simulations reveal the vacancy-driven enhancement in Na-ion diffusion of Ca-doped $Na_3PS_4$. Furthermore, the promising electrochemical performance of $TiS_2$/Na−Sn ASNBs employing $Na_{2.700}Ca_{0.150}PS_4$ is highlighted.

$Ca^{2+}$ is the most suitable divalent ion for substitution of $Na^+$ because of their similar ionic sizes ($Ca^{2+}$, 100 pm; $Na^+$, 102 pm). Figure 1a shows the X-ray diffraction (XRD) patterns of $Na_{3-2x}Ca_xPS_4$ prepared by a solid-state reaction at 700 °C. Without Ca doping ($x$ = 0.000), doublet peaks appear, which are indicative of the tetragonal phase. As the amount of Ca increases, however, the doublet peaks merge to become single peaks, reflecting the evolution of the cubic phase. However, these single peaks are asymmetric, implying the coexistence of cubic and tetragonal phases, which is later confirmed by X-ray Rietveld refinement analysis. As an unknown phase starts to evolve at $x$ = 0.450 (Figure S1), the doping range of Ca in $Na_3PS_4$ is determined to be $0 < x \leq 0.375$. Figure 1b presents the X-ray Rietveld refinement profile for $Na_{2.730}Ca_{0.135}PS_4$. All the peaks could be indexed to the cubic structure ($a$ = 6.9768(1) Å, $Z$ = 2, $I\bar{4}3m$, Table S1). The Rietveld refinement results for all the compositions are also provided in Figure S2 and Tables S2−S17. The refinement was performed by considering the coexistence of Ca-free t-$Na_3PS_4$ and Ca-doped c-$Na_3PS_4$ phases. Their crystal structures are shown in Figure S3. (To avoid confusion, Na sites in t-$Na_3PS_4$ are denoted $Na_t1$ and $Na_t2$.) The unit cell structure of Ca-doped c-$Na_3PS_4$ consists of a body-centered cubic sublattice of $PS_4^{3-}$ tetrahedra in which Na1 sites with higher occupancies and Na2 sites with lower occupancies are interconnected via 3D pathways (Figures 1c and S3). Ca occupies the Na1 site. As the amount of Ca increases, the lattice volume for Ca-doped c-$Na_3PS_4$ slightly decreases (∼1% for $Na_{2.730}Ca_{0.135}PS_4$, Figure S4 and Table S1), which could be explained by the slightly smaller ionic size of $Ca^{2+}$ than $Na^+$ and/or strong Coulombic attraction between $Ca^{2+}$ and $PS_4^{3-}$, and the decreased amounts of cations.

DFT calculations were performed to investigate the formation energies of undoped and Ca-doped $Na_3PS_4$ and



DOI: 10.1021/acsenergylett.8b01479
ACS Energy Lett. 2018, 3, 2504−2512

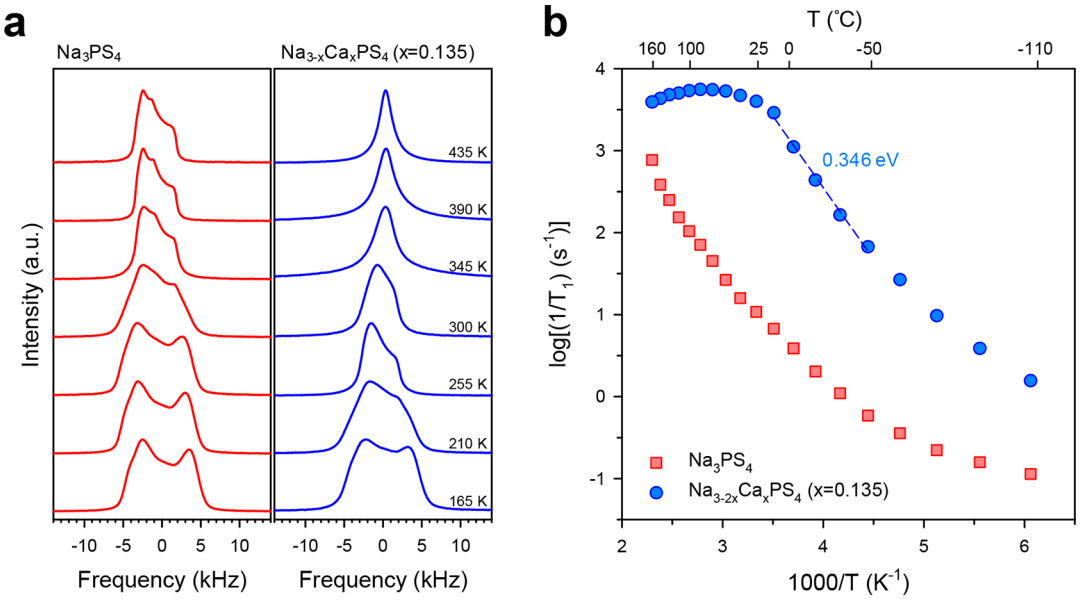


**Figure 2. Results of $^{23}$Na static NMR for t-$Na_3PS_4$ and Ca-doped c-$Na_3PS_4$ ($Na_{2.730}Ca_{0.135}PS_4$). (a) $^{23}$Na NMR spectra and (b) $^{23}$Na NMR spin−lattice relaxation rate $1/T_1$ at different temperatures.**

the corresponding $c/a$ ratios by varying the amount of Ca doped and the concentration of Na vacancies ($V_{Na}$) generated to compensate the higher charge of $Ca^{2+}$ (Figure 1d). The calculated $c/a$ ratio for the stoichiometric (pristine) t-$Na_3PS_4$ (without $V_{Na}$) is 1.021, which is in good agreement with the experimental observation (1.017). The calculated structures with different vacancy concentrations ($Na_{2.9375}PS_4$ and $Na_{2.875}PS_4$) and vacancy sites ($V^1_{Na_t}$ vs $V^2_{Na_t}$) maintain tetragonal geometries with $c/a$ = 1.017−1.031. On the other hand, $V_{Na}$ with Ca doping stabilizes the cubic structure. As shown in the triangles in Figure 1d (the red region of "Ca + $V_{Na}$", $Na_{2.750}Ca_{0.125}PS_4$), when Ca and $V_{Na}$ coexist, the $c/a$ ratio decreases to 0.995 and 0.98 (inverted triangles, Ca at the $Na_t2$ site and $V_{Na}$ at the $Na_t1$ site) with the most stable energies. Also, when more $V_{Na}$ is present (the blue region of "Ca + $2V_{Na}$", $Na_{2.625}Ca_{0.125}PS_4$, denoted as squares and diamonds), the structure better resembles the cubic geometry. The tetragonal-to-cubic phase transition might be associated with the interaction between $Ca^{2+}$ and $V_{Na}$. The detailed vacancy formation energies for undoped and Ca-doped $Na_3PS_4$ are also compared in Table 1. The formation energies for concurrent $V_{Na}$ and Ca doping ($Na_{2.750}Ca_{0.125}PS_4$: ∼0.6 eV) is approximately half of those for pure $V_{Na}$ ($Na_{2.9375}PS_4$, $Na_{2.8750}PS_4$: ∼1.0 eV), indicating the excellent Ca dopability with inducing $V_{Na}$ in $Na_3PS_4$. In particular, $V_{Na}$ was found to be the most stable near $Ca^{2+}$. Strong Coulombic repulsion between $Ca^{2+}$ and $Na^+$ prevents $Na^+$ from being located at the original Na sites close to $Ca^{2+}$, resulting in the generation of Na vacancies around $Ca^{2+}$.

Ca-doped $Na_3PS_4$ shows the excellent mechanical deformability (Figure S5). The electronic conductivities of $Na_{3-2x}Ca_xPS_4$, measured by the van der Pauw method, are $<10^{-8}$ S cm$^{-1}$.[10,13,39] $Na^+$ ionic conductivities were measured by the AC impedance method using ion-blocking Ti/$Na_{3-2x}Ca_xPS_4$/Ti symmetric cells. Their variation at 25 °C as a function of the amount of doped Ca ($x$) in a series of $Na_{3-2x}Ca_xPS_4$ prepared at 700 °C is displayed in Figure 1e (Nyquist and Arrhenius plots of conductivities are shown in the inset of Figures 1e and S6, respectively). t-$Na_3PS_4$ without Ca doping shows a conductivity of 0.077 mS cm$^{-1}$. This value is lower than that for c-$Na_3PS_4$ (0.2[8] or 0.1 mS cm$^{-1}$ in this work) but much higher than that for t-$Na_3PS_4$ in a previous report (∼0.001 mS cm$^{-1}$).[8] The discrepancy may stem from different Na vacancies, affected by experimental conditions.[26,29,40] As the amount of doped Ca ($x$) increases, the conductivity drastically increases and reaches a maximum value of 0.94 mS cm$^{-1}$ at $x$ = 0.135. This value is comparable to the conductivities of other state-of-the-art sulfide $Na^+$ superionic conductors (Table S18, characteristics for each material are also compared). Moreover, considering that the present result was achieved using cold-pressed pellets, even higher conductivity could be achieved if the grain-boundary resistance could be minimized using hot pressing or spark-plasma sintering.[35,36,41] The subsequent increase in the amount of doped Ca ($x$) results in a decrease in conductivity (e.g., 0.12 mS cm$^{-1}$ at $x$ = 0.30). Despite the conductivity enhancement by Ca doping, the activation energies for Ca-doped $Na_3PS_4$ (0.36−0.49 eV) are higher than that for other superionic conductors (typically, 0.2−0.3 eV)[4,8−10,13,27,34,37,41] and surprisingly even higher than that for t-$Na_3PS_4$ (0.35 eV), which will be discussed later. For the samples prepared at 550 °C, the Ca-doping-induced phenomena, the tetragonal-to-cubic phase transition and the concomitant conductivity enhancement along with increased activation energies are also confirmed (Figures S7 and S8).

The Arrhenius equation for conductivity is given by eq 1[42]

$$\sigma T = A_T \exp(-E_a/k_B T) \quad (1)$$

where $\sigma$ is the conductivity, $T$ the temperature in K, $A_T$ the pre-exponential factor proportional to the concentration of mobile ion carriers such as interstitials and vacancies $n_c$,[42] $E_a$ the activation energy (or activation barrier), and $k_B$ the Boltzmann constant.

The parabolic conductivity curve as a function of the amount of Ca doped ($x$) on $Na_{3-2x}Ca_xPS_4$ in Figure 1e reflects the variation in concentration of mobile ion carriers. Consistently, the as-obtained pre-exponential factors for $Na_{3-2x}Ca_xPS_4$ also follow the trend of $Na^+$ conductivities



DOI: 10.1021/acsenergylett.8b01479
ACS Energy Lett. 2018, 3, 2504−2512

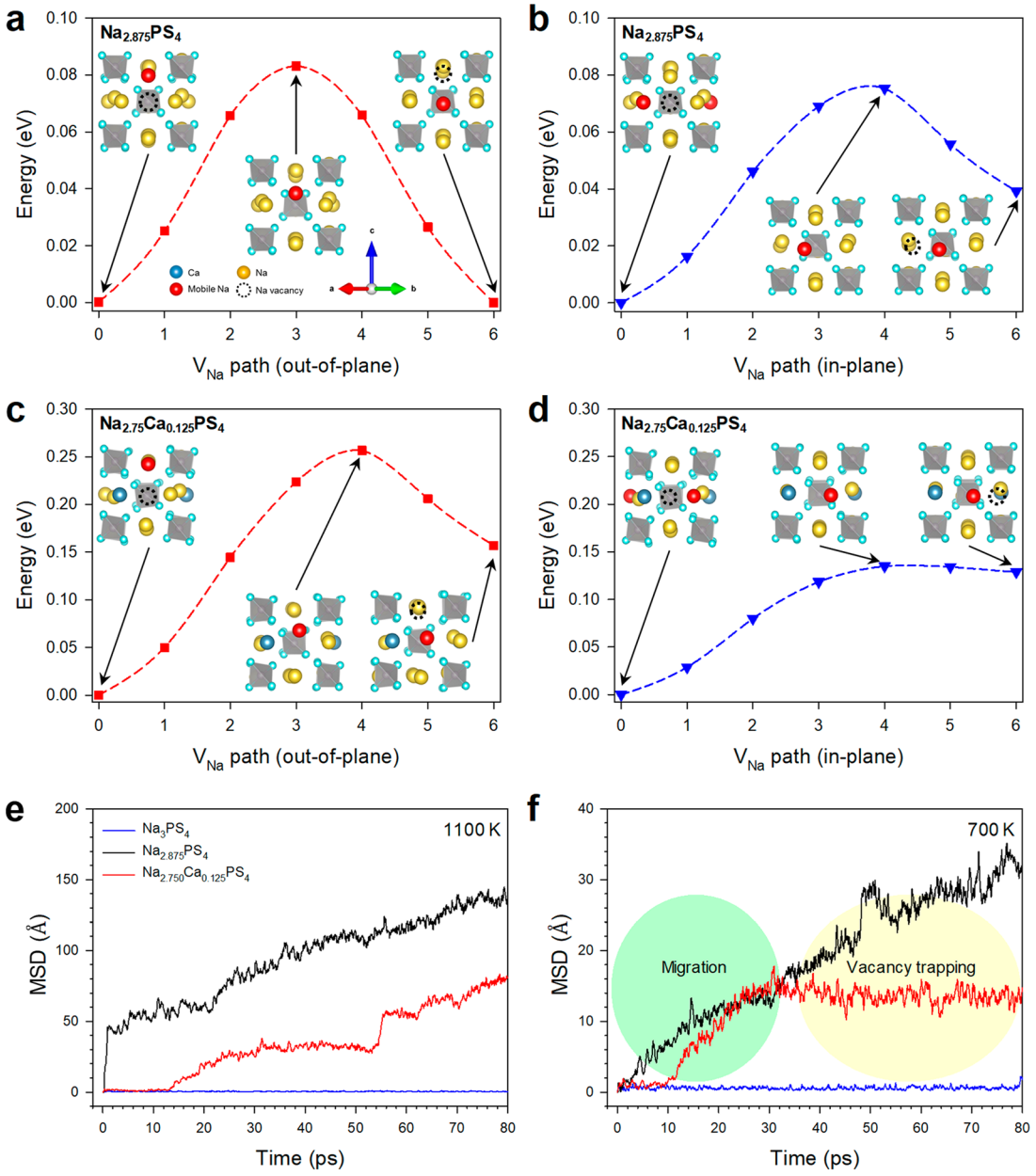


**Figure 3. Theoretical calculation results for undoped and Ca-doped $Na_3PS_4$. Calculated migration barriers for Na vacancies ($V_{Na}$) in undoped and Ca-doped $Na_3PS_4$ (a–d). The insets show the initial, transition, and final states. (a) Out-of-plane and (b) in-plane migration barriers for $Na_{2.875}PS_4$. (c) Out-of-plane and (d) in-plane migration barriers for $Na_{2.750}Ca_{0.125}PS_4$. MSD depending on the time step at (e) 1100 K and (f) 700 K.**

(Figure S8). A similar behavior is also found in the classical example of $Li_{4-3x}Al_xSiO_4$ ($0 \leq x \leq 0.5$).[42] Whereas the end members of the solid solution ($Li_4SiO_4$ and $Li_{2.5}Al_{0.5}SiO_4$ for which the specific $Li^+$ sites are fully occupied and empty, respectively) are almost insulating, the sample with the intermediate composition ($x$ = ~0.25) exhibits an optimal conductivity of ~$10^{-5}$ S $cm^{-1}$ at 100 °C.

$^{23}$Na solid-state NMR spectra for t-$Na_3PS_4$ and $Na_{2.730}Ca_{0.135}PS_4$ were obtained to acquire alternative information about Na-ion dynamics. Figure 2a displays $^{23}$Na static NMR spectra recorded at various temperatures. At a low temperature of 165 K, both spectra show broad complex asymmetric signals, which are attributed to second-order quadrupolar and dipolar interactions.[32] As the temperature increases, the broad spectra become narrower, which is referred to as motional narrowing.[32,43] Notably, for Ca-doped $Na_3PS_4$, at 345 K, the spectrum shows a symmetric peak. This suggests that Na-ion mobility is sufficiently high to average out the quadrupolar and dipolar interactions. In stark contrast, t-$Na_3PS_4$ shows an asymmetric resonance signal even at a high temperature of 435 K. Figure 2b shows $^{23}$Na NMR spin–lattice relaxation rates ($1/T_1$) as a function of temperature. For Ca-doped $Na_3PS_4$, $1/T_1$ exhibits a maximum at 360 K (~86 °C) at which the hopping frequency of $Na^+$ is regarded to be equivalent to the Larmor frequency $\omega_0$.[32,44] In contrast, $1/T_1$ for t-$Na_3PS_4$ does not reach the maximum value at 435 K, implying that Na-ion mobility in t-$Na_3PS_4$ at 435 K is still lower than the order of Larmor frequency.[32,44] In short, both the motional narrowing (Figure 2a) and spin–lattice relaxation rate results (Figure 2b) confirm much faster diffusion of $Na^+$ in



DOI: 10.1021/acsenergylett.8b01479
ACS Energy Lett. 2018, 3, 2504–2512

Ca-doped c-$Na_3PS_4$ than in t-$Na_3PS_4$, which agrees perfectly with the AC impedance results (Figure 1e).

The activation energy for Na-ion diffusion in Ca-doped $Na_3PS_4$, obtained from the slope of $\log[1/T_1]$ as a function of $1000/T$ (Figure 2b) at the low-temperature regime, is 0.346 eV.[32,44,45] Activation energy estimated at the low-temperature regime reflects localized ionic motion, whereas that from the high-temperature regime is determined by long-range ionic motion,[44,45] which is inaccessible in the present data. The value of 0.346 eV is lower than that obtained by the AC impedance method (0.49 eV, Figure 1e), which is reasonable considering the additional contributions involved in the AC impedance method, such as electrode−electrolyte interfacial and grain-boundary resistances.[18,32] Using the Einstein−Smoluchowski equation, a self-diffusion coefficient for Ca-doped $Na_3PS_4$ at 360 K, where $1/T_1$ reaches the maximum value, is calculated to be $1.4 \times 10^{-7}$ $cm^2$ $s^{-1}$.[32,44] The Nernst−Einstein relation then gives the corresponding ionic conductivity of 11 mS $cm^{-1}$. Using the Arrhenius equation with the activation energy of 0.346 eV, a conductivity of 1.4 mS $cm^{-1}$ at 25 °C is obtained (see the Supporting Information for details). Despite the rough estimation, interestingly, this value is comparable to that measured by the AC impedance method (0.94 mS $cm^{-1}$, Figure 1e).

For a majority of superionic conductors, ionic conductivities increase with decreasing energy barriers.[46,47] Highly polarizable elements, such as S and I, as a framework constituent are generally advantageous for fast ionic conduction because the energy barrier can be lowered.[42] Ceder and co-workers reported that body-centered cubic (bcc) anion frameworks allow direct hopping of $Li^+$ between adjacent tetrahedral sites with low energy barriers, enabling high ionic conductivities.[46] In a recent report, Mo and co-workers revealed significantly lowered energy barriers by concerted migrations of multiple ions, which rationalized the high ionic conductivities for non-bcc structured superionic conductors.[47] All the above-mentioned instances strongly emphasize the correlation between high conductivity and low energy barrier. In this regard, the result for Ca-doped $Na_3PS_4$, namely, the enhanced conductivities with increased energy barriers, is not common.

To understand this abnormal behavior of Ca-doped $Na_3PS_4$, the following theoretical methods were performed: (i) the nudged elastic band (NEB) method to examine the effect of $Ca^{2+}$ on the mobility of $Na^+$ locally distributed around $Ca^{2+}$ and (ii) DFTMD simulations to analyze the average macroscopic effect of $Ca^{2+}$ on the $Na^+$ mobility in the entire system.

As shown in Figure 3a,b, the $Na^+$ migration barriers along out-of-plane and in-plane directions for undoped $Na_3PS_4$ ($Na_{2.875}PS_4$) are quite low, ∼0.08 eV. In sharp contrast, the $Na^+$ migration barriers near $Ca^{2+}$ along out-of-plane and in-plane directions for Ca-doped $Na_3PS_4$ ($Na_{2.750}Ca_{0.125}PS_4$) are 2−3 times higher, 0.26 and 0.14 eV, respectively (Figure 3c,d). $Ca^{2+}$ has a more positive charge than $Na^+$, pushing away neighboring $Na^+$ because of strong Coulombic repulsion. Thus, Na vacancies are readily formed near $Ca^{2+}$ and easily trapped, resulting in a high migration barrier. The detailed information on the energy barriers for other paths is summarized in Figure S9 and Table S19.

Figure 3e,f shows the mean square distance (MSD) of total Na at 1100 and 700 K obtained by DFTMD simulations. As shown in Figure 3e, at 1100 K, the MSD for Ca-doped $Na_3PS_4$ ($Na_{2.750}Ca_{0.125}PS_4$, red) is much higher than that for pristine t-$Na_3PS_4$ having no $V_{Na}$ (blue). This result confirms that the large number of $V_{Na}$ created by Ca doping generates Na-ion pathways that facilitate $Na^+$ migration. This is also in line with the suggestion in a previous report that the conductivity of $Na_3PS_4$ is governed by the vacancies rather than the structure.[23,29,32−34] However, when t-$Na_3PS_4$ has the same $V_{Na}$ concentration ($Na_{2.875}PS_4$) as Ca-doped $Na_3PS_4$ ($Na_{2.750}Ca_{0.125}PS_4$), the MSD (black) of the former is relatively higher. This could be rationalized by the high energy barrier to $Na^+$ migration induced by $Ca^{2+}$. A similar tendency is found for $Na^+$ migration at 700 K. As shown in Figure 3f, the MSD for both undoped t-$Na_3PS_4$ having $V_{Na}$ ($Na_{2.875}PS_4$, black) and Ca-doped $Na_3PS_4$ ($Na_{2.750}Ca_{0.125}PS_4$, red) exhibits linearly increasing behaviors up to 30 ps. After 30 ps, however, the slope for Ca-doped $Na_3PS_4$ becomes zero, indicating a temporary trapping of Na vacancy, while that for undoped $Na_3PS_4$ keeps increasing linearly. These DFTMD simulation results match with the higher $Na^+$ migration barrier shown in the NEB results (Figures 3a−d and S9). Detailed MSD data for other temperatures are shown in Figure S10. It should also be noted that considering the much higher conductivities measured for Ca-doped $Na_3PS_4$ (maximum ∼1 mS $cm^{-1}$) than for t-$Na_3PS_4$ (0.077 mS $cm^{-1}$), in practice, t-$Na_3PS_4$ must have a much lower vacancy concentration than the one considered for the DFTMD simulations (4.17% corresponding to $Na_{2.875}PS_4$).

In short, by the complementary analysis so far, it could be rationalized that the overall conductivity can be determined by the interplay between the enhancement in $V_{Na}$ concentration generated by Ca doping and the impediment by the increased energy barriers near $Ca^{2+}$. It is believed that Ca-doped $Na_3PS_4$, showing high conductivities and high activation energies, is an exceptional case where the former (the enhancement in $V_{Na}$ concentration or the pre-exponential factor) prevails over the latter (the impediment by the increased energy barrier).

Electrochemical stability of Ca-doped $Na_3PS_4$ is assessed from the cyclic voltammetry test of Ti/$Na_{2.730}Ca_{0.135}PS_4$/$Na_3Sn$ cells in the negative (0.0−2.0 V (vs $Na/Na^+$)) and positive (1.5−5.0 V (vs $Na/Na^+$)) voltage ranges (Figure S11). Interestingly, Ca-doped $Na_3PS_4$ exhibits slightly poorer cathodic stability but better anodic stability than c-$Na_3PS_4$. The slightly deteriorated reduction stability by Ca-doping may be explained by possible formation of metallic Ca upon full reduction.[11]

Finally, $TiS_2$/Na−Sn ASNBs were fabricated using c-$Na_3PS_4$ (0.1 mS $cm^{-1}$) and Ca-doped $Na_3PS_4$ ($Na_{2.700}Ca_{0.150}PS_4$, ∼1 mS $cm^{-1}$) and cycled between 1.0 and 2.5 V at 30 °C (schematic of the all-solid-state cells are provided in Figure S12). Figure 4a shows the first two-cycle discharge−charge voltage profiles for the cell using Ca-doped $Na_3PS_4$ at 0.06C. The two voltage plateaus at ∼2.0 and 1.5 V during discharge agree with the previous report, which might be attributed to the irregular intercalation of $Na^+$ ions, followed by the formation of $Na_xTiS_2$.[48,49] The charge capacities at the second cycle for the cells using c-$Na_3PS_4$ and Ca-doped $Na_3PS_4$ are 191 and 198 mA h $g^{-1}$, respectively. These values, corresponding to an extraction of 0.8 mol of Na, are not only much higher than those for $TiS_2$-based ASNBs reported previously[27,34] but also comparable to those for $TiS_2$/Li cells using liquid electrolytes.[6,49] The charge capacities for $TiS_2$/Na−Sn cells employing c-$Na_3PS_4$ and Ca-doped $Na_3PS_4$ as a function of cycle number at different C-rates are also displayed in Figure 4b (voltage profiles at different C-rates and different


DOI: 10.1021/acsenergylett.8b01479
ACS Energy Lett. 2018, 3, 2504−2512

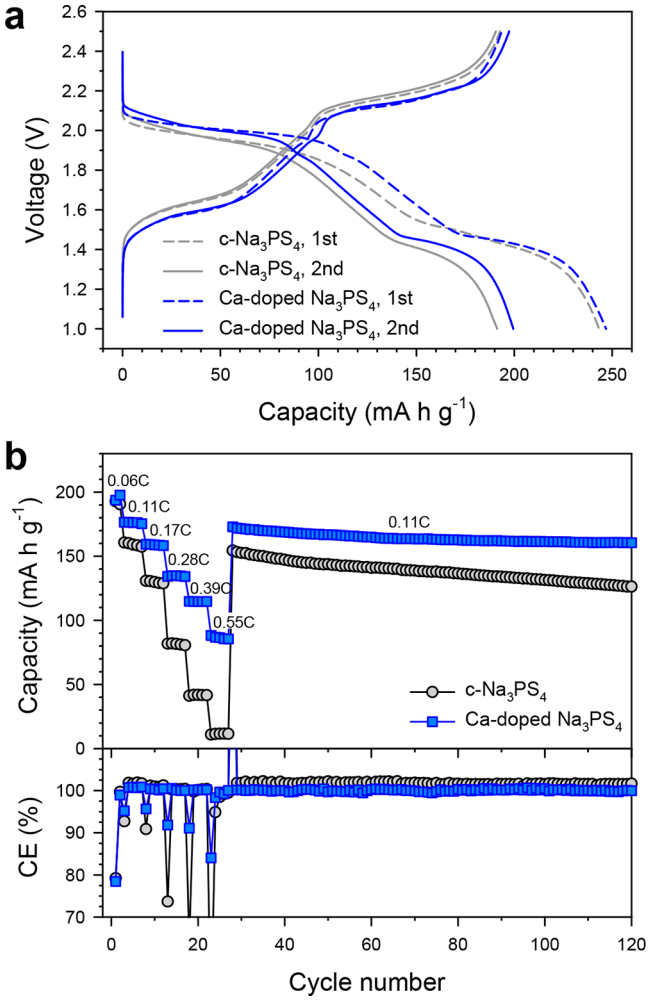


**Figure 4. Electrochemical performance of $TiS_2$/Na−Sn ASNBs using c-$Na_3PS_4$ and Ca-doped $Na_3PS_4$ ($Na_{2.700}Ca_{0.150}PS_4$) at 30 °C. (a) First two-cycle discharge−charge voltage profiles at 0.06*C*. (b) Charge capacity and the corresponding Coulombic efficiency (CE) as a function of cycle number at *C*-rates.**

cycle numbers are shown in Figure S13). At high *C*-rates, capacity difference varied by the solid electrolytes becomes distinct. At 0.55*C*, while the $TiS_2$/Na−Sn ASNB using c-$Na_3PS_4$ shows a negligible capacity of 11 mA h $g^{-1}$, the one using Ca-doped $Na_3PS_4$ retains 45% capacity (88 mA h $g^{-1}$), compared with that at 0.06*C*. Moreover, the capacity retention for the $TiS_2$/Na−Sn ASNB employing Ca-doped $Na_3PS_4$ after 100 cycles is 91.0%, which is in contrast to a retention of 78.6% achieved for the ASNB using c-$Na_3PS_4$. Overall, the decent electrochemical performance for the $TiS_2$/Na−Sn ASNB using Ca-doped $Na_3PS_4$ highlights the high $Na^+$ conductivity of Ca-doped $Na_3PS_4$ and the good compatibility between $TiS_2$ and Ca-doped $Na_3PS_4$.

In summary, new $Na^+$ superionic conductors, Ca-doped cubic $Na_3PS_4$ ($Na_{3-2x}Ca_xPS_4$ ($0 < x \leq 0.375$)), showing a maximum conductivity of ∼1 mS $cm^{-1}$ at 25 °C, were developed. It was shown that Ca substituted Na to form Na vacancies, which resulted in a tetragonal-to-cubic phase transition. The significant enhancement in $Na^+$-ionic conductivity of $Na_3PS_4$ by Ca doping along with the increased activation energy was confirmed by the AC impedance method and $^{23}Na$ NMR spectroscopy measurements. The NEB method and DFTMD calculations revealed that although the formation of Na vacancies by Ca doping caused the temporary trapping near $Ca^{2+}$, it resulted in an overall significant enhancement in the diffusion of $Na^+$ compared with that in vacancy-free $Na_3PS_4$. Finally, the high capacity and excellent cycling stability of $TiS_2$/Na−Sn ASNBs employing Ca-doped $Na_3PS_4$ ($Na_{2.700}Ca_{0.150}PS_4$) were successfully demonstrated. Our findings and developments are important in understanding the ionic conduction mechanism in superionic conductors and for designing new superionic conductors, thus contributing to progress in the field of all-solid-state batteries.

## ■ ASSOCIATED CONTENT

### Supporting Information

The Supporting Information is available free of charge on the ACS Publications website at DOI: 10.1021/acsenergylett.8b01479.

Experimental methods, conductivity obtained from $^{23}Na$ NMR results, formation energy from DFT, and supplementary results (PDF)

## ■ AUTHOR INFORMATION


### Corresponding Authors

*E-mail: yoonsjung@hanyang.ac.kr.
*E-mail: junhee@unist.ac.kr.

### ORCID

Seung-Tae Hong: 0000-0002-5768-121X
Yoon Seok Jung: 0000-0003-0357-9508


### Author Contributions

⊥C.K.M. and H.-J.L. contributed equally to this work. Y.S.J. conceived and led the project. C.K.M., K.H.P., and H.K. carried out the experiments. J.H.L., H.-J.L., K.C., H.Y., and M.-S.K. carried out the computation. C.K.M., J.W.H., Y.S.J., and S.-T.H. carried out the structural analysis. Y.S.J., J.H.L., C.K.M., and H.-J.L. wrote the manuscript. All authors contributed to discussions of the data analysis.

### Notes

The authors declare no competing financial interest.

## ■ ACKNOWLEDGMENTS

Y.S.J. was supported by the Technology Development Program to Solve Climate Changes and by Basic Science Research Program through the National Research Foundation of Korea (NRF) funded by the Ministry of Science, ICT & Future Planning (Nos. NRF-2017M1A2A2044501 and NRF-2018R1A2B6004996), and by KOREA HYDRO & NUCLEAR POWER CO., LTD (No. 2017-Tech-17). H.J.L. and J.H.L. were supported by Creative Materials Discovery Program through NRF (No. 2017M3D1A1040828).

## ■ REFERENCES


(1) Goodenough, J. B.; Park, K. S. The Li-Ion Rechargeable Battery: A Perspective. *J. Am. Chem. Soc.* **2013**, *135*, 1167−1176.
(2) Tarascon, J.-M. Key Challenges in Future Li-Battery Research. *Philos. Trans. R. Soc., A* **2010**, *368*, 3227−3241.
(3) Xu, K. Nonaqueous Liquid Electrolytes for Lithium-Based Rechargeable Batteries. *Chem. Rev.* **2004**, *104*, 4303−4418.
(4) Kato, Y.; Hori, S.; Saito, T.; Suzuki, K.; Hirayama, M.; Mitsui, A.; Yonemura, M.; Iba, H.; Kanno, R. High-Power All-Solid-State Batteries using Sulfide Superionic Conductors. *Nat. Energy* **2016**, *1*, 16030.
(5) Han, X.; Gong, Y.; Fu, K. K.; He, X.; Hitz, G. T.; Dai, J.; Pearse, A.; Liu, B.; Wang, H.; Rubloff, G.; et al. Negating Interfacial




DOI: 10.1021/acsenergylett.8b01479
*ACS Energy Lett.* 2018, 3, 2504−2512

Impedance in Garnet-Based Solid-State Li Metal Batteries. *Nat. Mater.* **2017**, *16*, 572−579.
(6) Yabuuchi, N.; Kubota, K.; Dahbi, M.; Komaba, S. Research Development on Sodium-Ion Batteries. *Chem. Rev.* **2014**, *114*, 11636−11682.
(7) Kundu, D.; Talaie, E.; Duffort, V.; Nazar, L. F. The Emerging Chemistry of Sodium Ion Batteries for Electrochemical Energy Storage. *Angew. Chem., Int. Ed.* **2015**, *54*, 3431−3448.
(8) Hayashi, A.; Noi, K.; Sakuda, A.; Tatsumisago, M. Superionic Glass-Ceramic Electrolytes for Room-Temperature Rechargeable Sodium Batteries. *Nat. Commun.* **2012**, *3*, 856.
(9) Banerjee, A.; Park, K. H.; Heo, J. W.; Nam, Y. J.; Moon, C. K.; Oh, S. M.; Hong, S.-T.; Jung, Y. S. $Na_3SbS_4$: A Solution Processable Sodium Superionic Conductor for All-Solid-State Sodium-Ion Batteries. *Angew. Chem., Int. Ed.* **2016**, *55*, 9634−9638.
(10) Jung, Y. S.; Oh, D. Y.; Nam, Y. J.; Park, K. H. Issues and Challenges for Bulk-Type All-Solid-State Rechargeable Lithium Batteries using Sulfide Solid Electrolytes. *Isr. J. Chem.* **2015**, *55*, 472−485.
(11) Wenzel, S.; Leichtweiss, T.; Weber, D. A.; Sann, J.; Zeier, W. G.; Janek, J. Interfacial Reactivity Benchmarking of the Sodium Ion Conductors $Na_3PS_4$ and Sodium $\beta$-Alumina for Protected Sodium Metal Anodes and Sodium All-Solid-State Batteries. *ACS Appl. Mater. Interfaces* **2016**, *8*, 28216−28224.
(12) Duchene, L.; Kuhnel, R.-S.; Stilp, E.; Reyes, E. C.; Remhof, A.; Hagemann, H.; Battaglia, C. A Stable 3 V All-Solid-State Sodium-Ion Battery Based on a Closo-Borate Electrolyte. *Energy Environ. Sci.* **2017**, *10*, 2609−2615.
(13) Park, K. H.; Bai, Q.; Kim, D. H.; Oh, D. Y.; Zhu, Y.; Mo, Y.; Jung, Y. S. Design Strategies, Practical Considerations, and New Solution Processes of Sulfide Solid Electrolytes for All-Solid-State Batteries. *Adv. Energy Mater.* **2018**, *8*, 1800035.
(14) Chi, X. W.; Liang, Y. L.; Hao, F.; Zhang, Y.; Whiteley, J.; Dong, H.; Hu, P.; Lee, S.; Yao, Y. Tailored Organic Electrode Material Compatible with Sulfide Electrolyte for Stable All-Solid-State Sodium Batteries. *Angew. Chem., Int. Ed.* **2018**, *57*, 2630−2634.
(15) Kim, J.-J.; Yoon, K.; Park, I.; Kang, K. Progress in the Development of Sodium-Ion Solid Electrolytes. *Small Methods* **2017**, *1*, 1700219.
(16) Yang, Z.; Zhang, J.; Kintner-Meyer, M. C. W.; Lu, X.; Choi, D.; Lemmon, J. P.; Liu, J. Electrochemical Energy Storage for Green Grid. *Chem. Rev.* **2011**, *111*, 3577−3613.
(17) Zheng, J.; Tang, M.; Hu, Y.-Y. Lithium Ion Pathway within $Li_7La_3Zr_2O_{12}$-Polyethylene Oxide Composite Electrolytes. *Angew. Chem., Int. Ed.* **2016**, *55*, 12538−12542.
(18) Park, K. H.; Oh, D. Y.; Choi, Y. E.; Nam, Y. J.; Han, L.; Kim, J.-Y.; Xin, H.; Lin, F.; Oh, S. M.; Jung, Y. S. Solution-Processable Glass LiI-$Li_4SnS_4$ Superionic Conductors for All-Solid-State Li-ion Batteries. *Adv. Mater.* **2016**, *28*, 1874−1883.
(19) Heo, J. W.; Banerjee, A.; Park, K. H.; Jung, Y. S.; Hong, S.-T. New Na-Ion Solid Electrolytes $Na_{4-x}Sn_{1-x}Sb_xS_4$ ($0.02 \leq x \leq 0.33$) for All-Solid-State Na-Ion Batteries. *Adv. Energy Mater.* **2018**, *8*, 1702716.
(20) Kim, T. W.; Park, K. H.; Choi, Y. E.; Lee, J. Y.; Jung, Y. S. Aqueous-Solution Synthesis of $Na_3SbS_4$ Solid Electrolytes for All-Solid-State Na-Ion Batteries. *J. Mater. Chem. A* **2018**, *6*, 840−844.
(21) Jansen, M.; Henseler, U. Synthesis, Structure Determination, and Ionic Conductivity of Sodium Tetrathiophosphate. *J. Solid State Chem.* **1992**, *99*, 110−119.
(22) Tanibata, N.; Noi, K.; Hayashi, A.; Kitamura, N.; Idemoto, Y.; Tatsumisago, M. X-ray Crystal Structure Analysis of Sodium-Ion Conductivity in $94Na_3PS_4 \bullet 6Na_4SiS_4$ Glass-Ceramic Electrolytes. *ChemElectroChem* **2014**, *1*, 1130−1132.
(23) Zhu, Z.; Chu, I.-H.; Deng, Z.; Ong, S. P. Role of $Na^+$ Interstitials and Dopants in Enhancing the Cubic $Na_3PS_4$ Superionic Conductor. *Chem. Mater.* **2015**, *27*, 8318−8325.
(24) Tanibata, N.; Noi, K.; Hayashi, A.; Tatsumisago, M. Preparation and Characterization of Highly Sodium Ion Conducting $Na_3PS_4$-$Na_4SiS_4$ Solid Electrolytes. *RSC Adv.* **2014**, *4*, 17120−17123.
(25) Wang, H.; Chen, Y.; Hood, Z. D.; Sahu, G.; Pandian, A. S.; Keum, J. K.; An, K.; Liang, C. An Air-Stable $Na_3SbS_4$ Superionic Conductor Prepared by a Rapid and Economic Synthetic Procedure. *Angew. Chem., Int. Ed.* **2016**, *55*, 8551−8555.
(26) Park, K. H.; Kim, D. H.; Kwak, H.; Jung, S. H.; Lee, H.-J.; Banerjee, A.; Lee, J. H.; Jung, Y. S. Solution-Derived Glass-Ceramic NaI·$Na_3SbS_4$ Superionic Conductors for All-Solid-State Na-Ion Batteries. *J. Mater. Chem. A* **2018**, *6*, 17192−17200.
(27) Yu, Z.; Shang, S.-L.; Seo, J.-H.; Wang, D.; Luo, X.; Huang, Q.; Chen, S.; Lu, J.; Li, X.; Liu, Z.-K.; Wang, D. Exceptionally High Ionic Conductivity in $Na_3P_{0.62}As_{0.38}S_4$ with Improved Moisture Stability for Solid-State Sodium-Ion Batteries. *Adv. Mater.* **2017**, *29*, 1605561.
(28) Zhang, L.; Yang, K.; Mi, J.; Lu, L.; Zhao, L.; Wang, L.; Li, Y.; Zeng, H. Solid Electrolytes: $Na_3PSe_4$: A Novel Chalcogenide Solid Electrolyte with High Ionic Conductivity. *Adv. Energy Mater.* **2015**, *5*, 1501294.
(29) Bo, S.-H.; Wang, Y.; Kim, J. C.; Richards, W. D.; Ceder, G. Computational and Experimental Investigations of Na-Ion Conduction in Cubic $Na_3PSe_4$. *Chem. Mater.* **2016**, *28*, 252−258.
(30) Duchardt, M.; Ruschewitz, U.; Adams, S.; Dehnen, S.; Roling, B. Vacancy-Controlled $Na^+$ Super ion Conduction in $Na_{11}Sn_2PS_{12}$. *Angew. Chem., Int. Ed.* **2018**, *57*, 1351−1355.
(31) Zhang, Z.; Ramos, E.; Lalère, F.; Assoud, A.; Kaup, K.; Hartman, P.; Nazar, L. F. $Na_{11}Sn_2PS_{12}$: A New Solid State Sodium Superionic Conductor. *Energy Environ. Sci.* **2018**, *11*, 87−93.
(32) Yu, C.; Ganapathy, S.; de Klerk, N. J. J.; van Eck, E. R. H.; Wagemaker, M. Na-Ion Dynamics in Tetragonal and Cubic $Na_3PS_4$, A Na-Ion Conductor for Solid State Na-Ion Batteries. *J. Mater. Chem. A* **2016**, *4*, 15095−15105.
(33) de Klerk, N. J. J.; Wagemaker, M. Diffusion Mechanism of the Sodium-Ion Solid Electrolyte $Na_3PS_4$ and Potential Improvements of Halogen Doping. *Chem. Mater.* **2016**, *28*, 3122−3130.
(34) Chu, I. H.; Kompella, C. S.; Nguyen, H.; Zhu, Z. Y.; Hy, S.; Deng, Z.; Meng, Y. S.; Ong, S. P. Room-Temperature All-solid-state Rechargeable Sodium-ion Batteries with a Cl-doped $Na_3PS_4$ Superionic Conductor. *Sci. Rep.* **2016**, *6*, 33733.
(35) Aboulaich, A.; Bouchet, R.; Delaizir, G.; Seznec, V.; Tortet, L.; Morcrette, M.; Rozier, P.; Tarascon, J. M.; Viallet, V. A New Approach to Develop Safe All-Inorganic Monolithic Li-Ion Batteries. *Adv. Energy Mater.* **2011**, *1*, 179.
(36) Kali, R.; Mukhopadhyay, A. Spark Plasma Sintered/Synthesized Dense and Nanostructured Materials for Solid-State Li-Ion Batteries: Overview and Perspective. *J. Power Sources* **2014**, *247*, 920−931.
(37) Richards, W. D.; Tsujimura, T.; Miara, L. J.; Wang, Y.; Kim, J. C.; Ong, S. P.; Uechi, I.; Suzuki, N.; Ceder, G. Design and Synthesis of the Superionic Conductor $Na_{10}SnP_2S_{12}$. *Nat. Commun.* **2016**, *7*, 11009.
(38) Zhang, L.; Zhang, D.; Yang, K.; Yan, X.; Wang, L.; Mi, J.; Xu, B.; Li, Y. Vacancy-Contained Tetragonal $Na_3SbS_4$ Superionic Conductor. *Adv. Sci.* **2016**, *3*, 1600089.
(39) van der Pauw, L. J. A Method of Measuring the Resistivity and Hall Coefficient on Lamellae of Arbitrary Shape. *Philips Technol. Rev.* **1958**, *20*, 220−224.
(40) Krauskopf, T.; Culver, S. P.; Zeier, W. G. Local Tetragonal Structure of the Cubic Superionic Conductor $Na_3PS_4$. *Inorg. Chem.* **2018**, *57*, 4739−4744.
(41) Seino, Y.; Ota, T.; Takada, K.; Hayashi, A.; Tatsumisago, M. A Sulphide Lithium Super Ion Conductor is Superior to Liquid Ion Conductors for Use in Rechargeable Batteries. *Energy Environ. Sci.* **2014**, *7*, 627−631.
(42) Bruce, P. G. *Solid State Electrochemistry*; Cambridge University: New York, 1995.
(43) Hendrickson, J. R.; Bray, P. J. Nuclear Magnetic Resonance Studies of $^7$Li Ionic Motion in Alkali Silicate and Borate Glasses. *J. Chem. Phys.* **1974**, *61*, 2754.
(44) Uitz, M.; Epp, V.; Bottke, P.; Wilkening, M. Ion Dynamics in Solid Electrolytes for Lithium Batteries. *J. Electroceram.* **2017**, *38*, 142−156.


DOI: 10.1021/acsenergylett.8b01479
*ACS Energy Lett.* 2018, 3, 2504−2512

(45) Kuhn, A.; Kunze, M.; Sreeraj, P.; Wiemhofer, H. D.; Thangadurai, V.; Wilkening, M.; Heitjans, P. NMR Relaxometry as a Versatile Tool to Study Li Ion Dynamics in Potential Battery Materials. *Solid State Nucl. Magn. Reson.* **2012**, *42*, 2−8.
(46) Wang, Y.; Richards, W. D.; Ong, S. P.; Miara, L. J.; Kim, J. C.; Mo, Y.; Ceder, G. Design Principle for Solid-State Lithium Superionic Conductors. *Nat. Mater.* **2015**, *14*, 1026−1031.
(47) He, X.; Zhu, Y.; Mo, Y. Origin of Fast Ion Diffusion in Super-Ionic Conductors. *Nat. Commun.* **2017**, *8*, 15893.
(48) Newman, G. H.; Klemann, L. P. Ambient Temperature Cycling of an Na-$TiS_2$ Cell. *J. Electrochem. Soc.* **1980**, *127*, 2097−2099.
(49) Ryu, H. S.; Kim, J. S.; Park, J. S.; Park, J. W.; Kim, K. W.; Ahn, J. H.; Nam, T. H.; Wang, G. X.; Ahn, H. J. Electrochemical Properties and Discharge Mechanism of Na/$TiS_2$ Cells with Liquid Electrolyte at Room Temperature. *J. Electrochem. Soc.* **2013**, *160*, A338−A343.



DOI: 10.1021/acsenergylett.8b01479
*ACS Energy Lett.* 2018, 3, 2504−2512